Journal of
Materials Chemistry A

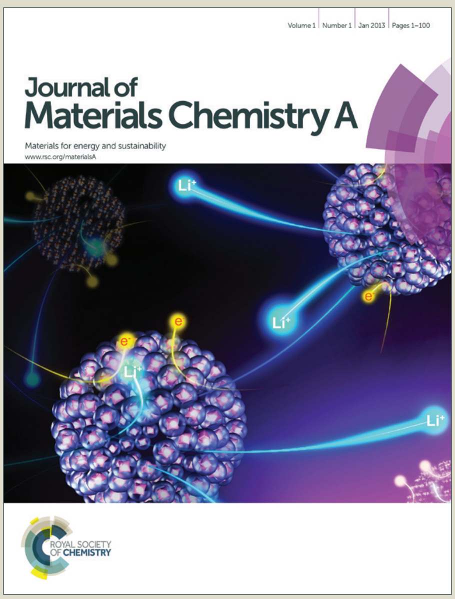

Journal Name

ARTICLE

The Influence of the Mesoporous TiO_2 Scaffold in the Performance of Methyl Ammonium Lead Iodide (MAPI) Perovskite solar cells: Charge Injection, Charge Recombination and Solar Cell Efficiency Relationship.

Received 00th January 20xx,
Accepted 00th January 20xx

DOI: 10.1039/x0xx00000x

www.rsc.org/

Alba Matas Adams[a], Jose Manuel Marin-Beloqui[a], Georgiana Stoica[a]* and Emilio Palomares* [a,b]

Methyl Ammonium Lead Iodide (MAPI) perovskite solar cells have achieved over 20% light-to-energy conversion efficiency with the use of a thin mesoporous layer of TiO_2 as scaffold for the MAPI. Although other solar cell configurations have been also reported, so far only those containing the mesoporous TiO_2 ($mpTiO_2$) have achieved such performance. Herein we describe an exhaustive study of the effects, over the MAPI solar cell performance, of different synthetic routes to achieve the nanocrystalline TiO_2 nanoparticles that are used to fabricate the mpTiO2 layer. Furthermore, we also measured the interfacial charge transfer dynamics to elucidate the device function-charge recombination kinetics relationship in the different type of synthesised $mpTiO_2$. Our results show that the choice of the chemical properties of the $mpTIO_2$ layer is of utmost importance to achieve high solar-to-energy conversion efficiencies with remarkable effects over the measured charge carrier recombination kinetics.

Introduction

The research of earth abundant and inexpensive materials for solar cells such as MAPI[1, 2], SnS[3] and CZTS[4] is attracting much attention and hold the promise to fill the gap of the terawatt solar energy production.[5]

In less than 5 years the reported efficiency for MAPI perovskite solar cells has arrived to overpass 20% under standard conditions (100mW/cm^2 sun-simulated 1.5 AM G)[6].

Although the interest in MAPI, as photoactive material, in solar cells has derived in multiple solar cell configurations[7], with solar cell efficiencies superior to other related energy conversion devices such as dye sensitized solar cells, organic solar cells and quantum dot solar cells, the most utilised configuration is the one that uses mesoporous TiO_2 ($mpTiO_2$) as scaffold and/or contact electrode. In fact, the best reported efficiencies have been published with the following device configuration: FTO/$dTiO_2$/$mTiO_2$/MAPI or MAPIC/ HTM/Au where FTO is fluorine doped tin oxide, $dTiO_2$ is a thin and dense layer of TiO_2, $mpTiO_2$ is the mesoporous layer of TiO_2, MAPI or MAPIC is the methyl ammonium lead iodide without or with chloride, respectively, HTM is the hole transport material and Au is the gold metal contact.

Mesoporous TiO_2 has been widely used in different areas such as catalysis[8], sensing[9] and energy[10]. In the later area of research, energy, the TiO_2 is paramount in so called Grätzel solar cells[11] or dye sensitized solar cells (DSSC) with an outstanding number of reports on the properties of the $mpTiO_2$ and its effects over the DSSC performance[12-14]. In contrast, in MAPI solar cells the number of such studies is scarce for several reasons; including the considerable recent discover of MAPI solar cells and the fact that MAPI solar cells can also be constructed without the use of $mpTiO_2$ with a noteworthy efficiency[15, 16]. Nonetheless, there are important scientific questions that are still under debate in relation with the role of the nanocrystalline TiO_2 nanoparticles and, hence, the $mpTiO_2$ layer over the MAPI device function. For example, taking into account that MAPI solar cells also work well using $mpAl_2O_3$ as scaffold and the Al_2O_3 is a well-known wide band-gap insulator, is not clear if it is really necessary an efficient electron transfer reaction from the MAPI perovskite material to the TiO_2 conduction band, TiO_2 CB; (so called charge injection in a parallelism with the charge transfer from the dye excited state to the TiO_2 CB in DSSC) or if the electron accumulation at the $mpTiO_2$ plays a role on the MAPI solar cell voltage at all.

In this work we aim to study how different $mpTiO_2$ layers fabricated using different synthetic routes[12] effect a change on the MAPI solar cell parameters (short circuit current, Isc, open circuit voltage, Voc, fill factor, FF and the overall efficiency, η). The synthetic routes differ on the pH synthetic conditions leading to an acid route and a basic route and their respective

a. Institute of Chemical Research of Catalonia (ICIQ). Avda. Països Catalans, 16. Tarragona E-43007. Spain
b. ICREA. Passeig Lluís Companys, 18. Barcelona. E-08020. Spain

† Footnotes relating to the title and/or authors should appear here. Electronic Supplementary Information (ESI) available: [details of any supplementary information available should be included here]. See DOI: 10.1039/x0xx00000x

acid or basic TiO_2 pastes used to fabricate the $mpTiO_2$. Moreover, we examined the electrical differences of the different MAPI perovskite solar cells in terms of charge density (defined as the total accumulated charge at the solar cell) as a function of light bias (cell voltage due to external applied light at different and controlled light intensities) and its relation with capacitance and carrier recombination lifetime measured under solar cell working conditions.

Experimental Section

Nanocrystalline TiO_2 nanoparticles ($ncTiO_2$) synthesis.

The colloids of titanium dioxide nanoparticles were obtained starting from the same precursor (titanium isopropoxide), but different peptidization agents were used to modify the surface charge. Two different synthetic routes were followed as previously reported by Hore et al[12].

Acid Route

The acid preparation of TiO_2 nanocrystalline nanoparticles consisted on 20mL of anhydrous titanium isopropoxide (Sigma Aldrich© 97%) mixed under argon atmosphere with 5.5 mL of glacial acetic acid (Panreac©) and stirred for 10 minutes.

In a separated Erlenmeyer, 120 mL of a 0.1 M nitric acid solution (Scharlau, 69.5%) in distilled water was degassed with argon.

The TiO_2 colloidal solution was injected dropwise at room temperature while stirring.

The final mixture was stirred vigorously under argon at 1500 rpm for 10 minutes, and finally heated in air for 8 hours at 80°C, followed by room temperature cooling over night.

Next, the solution was filtrated at room temperature using a 0.45 µm syringe filter.

To allow the $ncTiO_2$ to grow into the desired particle size, 5% in weight of the $ncTiO_2$ solution was autoclaved at 220°C for 12 hours and later allowed to cool down to room temperature. The obtained particles sizes were between 15-20nm.

The colloids were dispersed with a 60 seconds cycle burst using a sonic probe horn, and concentrated to 12.5% in TiO_2 weight to prepare the acid $mpTiO_2$ paste for the MAPI perovskite solar cell fabrication.

Basic Route

A similar procedure was followed for the basic peptidization, but instead of mixing the titanium isopropoxide with acetic acid the 20 mL were injected dropwise into a 0.1M solution of tetramethylammonium hydroxide (Sigma Aldrich©, 25wt% in H_2O) in distilled water previously degassed with argon. The solution was vigorously stirred at 1500 rpm for 10 minutes and then heated at 80°C, 500 rpm for 8h.

Next, the solution was left to cool down over night, filtrated as mentioned above and recovered.

For the basic route, the procedure to grow the nanoparticles is alike the acid route but the autoclave temperature is set to 180°C

In both cases, to form the titanium dioxide pastes from the $ncTiO_2$, we added 6.2 w% of Poly (ethylene oxide) (Sigma Aldrich©, molecular weight (Mw)≈300000) to the final suspension.

Nanocrystalline TiO_2 nanoparticles characterization.

The nanocrystalline TiO_2 particles were characterized using XRD (X-ray powder diffraction), TEM (transmission electron microscopy), nitrogen isotherms (Brunauer-Emmett-Teller) and Z potential measurements as shown.

Powder XRD was measured in a Bruker© AXS D8 Advance diffractometer equipped with a Cu tube, a Ge (111) incident beam monochromator, and a Vantec-1 PSD. Data were recorded in the range 5-70° 2θ with an angular step size of 0.016° and a counting time of 6 seconds per step.

Transmission Electron Microscopy (TEM) was carried out in a JEOL JEM-1011 microscope operating at 100 kV and equipped with a SIS Megaview III CCD camera. A 5µL of the sample suspended in ethanol were placed on a carbon-coated copper grids followed by evaporation at ambient conditions.

Zeta potential (ζ-potential) was measured with a NanoSizer (MALVERN© Nano-ZS) using dynamic light scattering (DLS) and the Smoluchowski equation. All measurements were performed at 25°C.

Nitrogen isotherms (BET) measurements were carried out at 77K on a Quantachrome Autosorb© iQ analyser. Prior to the analysis, the samples were degassed in a vacuum at 300 °C for 5h. The BET theory was applied to calculate the total surface area.

MAPI perovskite solar cell fabrication and characterization

The device presents the following architecture: FTO/d-TiO_2/mp-TiO_2/MAPI/OMeTAD/gold, and for its preparation a thin (50 nm) and dense titanium oxide layer (d-TiO_2) was deposited by spin-coating onto the Fluorine doped Tin Oxide glass (FTOs) with a resistance of 8 Ω/cm^2 as previously described.[17]

To homogenize this layer, the substrates were immersed in a 40mM $TiCl_4$ solution at 70°C for 30 minutes and annealed at 500°C for 20 minutes.

Next, the mesoporous titanium oxide layer (mp-TiO_2) was spin-coated, and in this case, three different pastes of titanium oxide were used: Commercial paste (Ti Nanoxide HT/SP Solaronix©), Acid paste and Basic Paste, in different proportions of paste: ethanol, to obtain a mesoporous TiO_2 layer of 400 nm. The substrates were then heated at 325°C for 30 minutes, 375°C for 5 minutes, 450°C for 15 minutes and at 500°C for 30 minutes.

For the MAPI perovskite preparation, methyl ammonium iodide (MAI) synthesized as described previously[18] was mixed with lead chloride ($PbCl_2$) (Sigma Aldrich©, 98%) in a 3:1 molar ratio in DMF (anhydrous dimethyl formamide) and deposited over the different mp-TiO_2 film in a glove box ([H_2O]<0.1ppm and [O_2]<100ppm) at 2000 rpm for 60 seconds.

Next, the film was annealed at 100°C for 1 hour.

The Hole Transport Material (HTM) spiro-OMeTAD (1-Material©) was dissolved in chlorobenzene (70mg/mL). Bis (trifluoromethane)-sulfonimide lithium salt (520mg/mL) and 4-tertbutylpiridine were used as chemical additives.

For all different devices we kept identical spin-coating conditions.

Finally, an 80 nm layer of gold was evaporated as anode by thermal evaporation at a pressure close to $1X10^{-6}$ mbar.

Photo-induced characterization.

Several techniques have been used to characterise either $mpTiO_2$/MAPI and $mpTiO_2$/MAPI/OMeTAD thin films or complete MAPI perovskite solar cells.

Picosecond-nanosecond Time Correlated Single Photon Counting (ps-ns TCSPC) was used to estimate charge injection and measure the radiate recombination lifetime. The system used was an Edinburgh Instruments© LifeSpec-II spectrometer with a PMT detector and a laser excitation source with a nominal wavelength of 470 nm and an IR (Instrument Response) measured at FWHM (Full width at half maximum) of 400 ps.

Photo-induced charge recombination kinetics in thin films was carried out using a home-build L-TAS system (Laser Transient Absorption Spectroscopy) that consist in a Nd-YAG excitation source in line with an optical parametric oscilator (OPO) to tune the excitation wavelength with a laser pulse energy of $75microJ/cm^2$. The probe wavelength is a 150 W lamp that is filtered through two monochromators from Dongwoo Optron (DM500i model) positioned in front and behind the sample holder. The signal is recorded using an InGAs photodiode for the IR region.

Photo-induced differential charging (PIDC) was used to register the charge accumulated at the solar cell under different light bias. The PIDC technique was used as described before[17]. In brief, PIDC uses the photo-induced transient photocurrent decay (PIT-PC) and the PIT-PV decays to calculate the solar cell capacitance assuming two caveats: (1) the charge losses at short circuit in the solar cell under illumination are negligible and (2) the solar cell Isc value is linear with the increase of sun-simulated light intensity. The first caveat can be tested by measuring PIT-PC in the dark and at 1 sun conditions and compare that there are not critical differences in both decays. The second caveat can be tested measuring the MAPI solar cell under different light intensity conditions and registering the Isc. The relationship between Isc and light intensity (LI) must be close to α=1 where α is the exponential factor in the power law relationship $P \propto LI^{\alpha}$

The photo-induced transient photovoltage (PIT-PV) was measured using a rig of white LEDs plus a nanosecond PTI GL-3300 N_2 dye laser[19]. Once the MAPI solar cell voltage has arrived to equilibrium, for a given light bias, a short laser pulse given by the N_2 dye laser produced a small charge in Voc (usually less than 20mV). The original Voc is restored after the N_2 dye laser pulse. The generated voltage decay, thus, represents a small ΔV at a give light bias that can be directly correlated with the device charge measured at the same given light bias (Voc).

Results and discussion

Nanocrystalline TiO_2 nanoparticles ($ncTiO_2$).

Figure 1 illustrates the TEM (Transmission Electron Microscopy) images for the acid, the basic and a commercial sample of $ncTiO_2$ particles. As can be seen, the acid route leads to smaller $ncTiO_2$ with a more spherical shape than the presented in the case of the basic nanoparticles that have a rod-like shape and bigger size.

The X-ray diffraction (XRD) measurements (Figure 2) shows clear diffraction peaks at 2 tetha angle (2θ) at 25° and 48° indicating TiO_2 anatase phase, in good agreement with the standard spectrum (JCPDS: 84-1286). Moreover, it can be seen that for the basic $ncTiO_2$ the diffraction pattern is more resolved in sharp peaks in contrast with the acid $ncTiO_2$ samples but in this case is due to the small size of the acid TiO_2 nanoparticles.

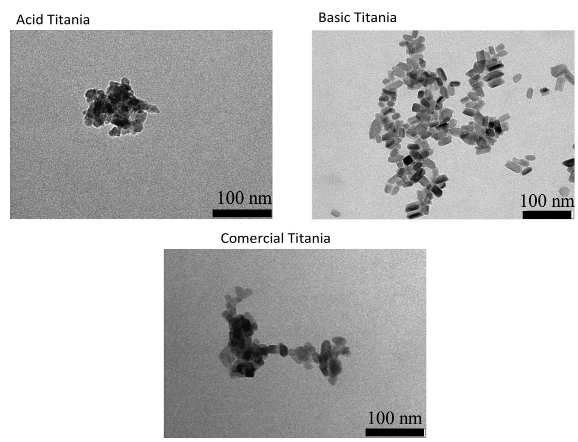

Figure 1. TEM images of ncTiO2 from different synthetic routes. The scale bar is 100nm.

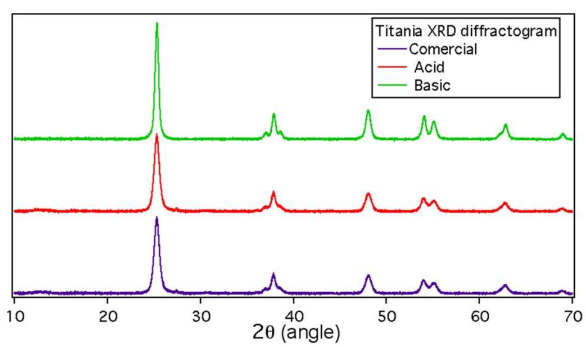

Figure 2. XRD measurements for $ncTiO_2$ acid samples (red) and the $ncTiO_2$ basic samples (green).

We carried out further analysis of the samples measuring the zeta potential and the surface area. The zeta potential is a key measurement to evaluate the different charge at the surface of the $ncTiO_2$ particles. Table 1 shows the different properties for the $ncTiO_2$ samples studied in the present work.

Table 1. NcTiO2 characterisation parameters.

	Size (nm)	S_{BET} (m^2/g)	V_{pore} (cm^3/g)	PSD (nm)	Zpot (mV)
Acid	**10-20**	**92**	**0.2**	**8.46**	**-14.6**
Basic	**15-30**	**49**	**0.11**	**9.33**	**-24.8**
Com	**10-20**	**85**	**0.48**	**22.6**	**-3.53**

S_{BET}= Surface area measurement. V_{pore} = Pore volume. PSD=Pore Size Distribution. Zpot= Zeta potential. Com= commercial sample.

Thus, as can be seen from Figure 1 and Figure 2, as well as, from the parameters listed in Table 1 there are important differences on the ncTiO$_2$ particles depending on the synthetic route. For example, the different Zeta potential can be correlated with different pH values for the mpTiO$_2$ paste as demonstrated before.[20] The acid paste with a -14.6 mV will correspond to a pH value of 6.5, while for the case of the basic paste, -24.8mV corresponds to a pH of 7.5, which is neutral pH.

Once the ncTiO$_2$ were characterised we prepared mpTiO$_2$ thin films alike those ones that will be used for the fabrication of the solar cells and performed the initial characterization of two of the interfacial charge transfer reactions that occur at the solar cell as detailed in the next point.

Charge injection in mpTiO$_2$/MAPI thin films and charge recombination in mpTiO2/MAPI and mp/TiO2/OMeTAD thin films.

On the one hand, we measured the charge injection from the MAPI perovskite into the TiO$_2$ CB using TCSPC as detailed in the Experimental section. The TCSPC is commonly used to scrutinize the radiative recombination lifetime in MAPI and MAPIC thin films[21, 22] and has been useful to evaluate the radiative charge recombination order[23]. Here we used the TCSPC measurements to measure the changes on the MAPI perovskite radiative recombination lifetime. Figure 3 illustrates the different photoluminescence decays for the different mpTiO$_2$/MAPI films.

As can be appreciated the MAPI perovskite radiative recombination lifetime is greatly affected upon the different mpTiO$_2$ film. It is worthy to mention that we have also used mpAl$_2$O$_3$ for comparison purposes and all films have equivalent absorbance at the excitation wavelength (λex=470nm).

The slower decay lifetime for the pastes corresponds to the basic mpTiO$_2$ with a value of τ1=47ns and τ2=6ns, in contrast with the acid mpTiO$_2$ that has a decay lifetime of τ1=30ns and τ2=5ns. These values appear to be faster than those values reported for other MAPI films[23].

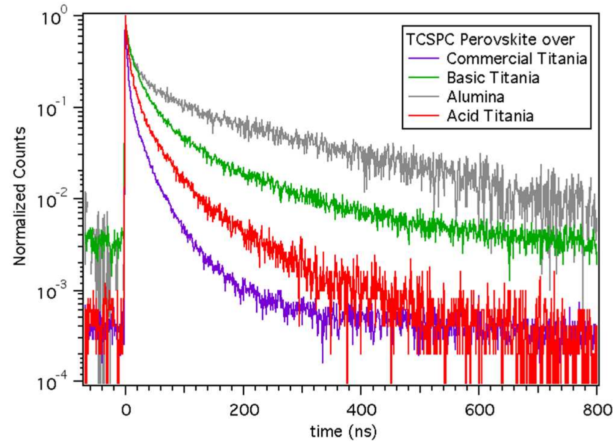

Figure 3. Normalised photoluminescence decays measured after excitation at λ=470nm under nitrogen and monitoring at 750 nm.

On the other hand, we used IR L-TAS to measure the interfacial charge recombination in mpTiO$_2$/MAPI/spiro-OMeTAD films. Upon light excitation the MAPI perovskite generates free carriers (electrons and holes) and can transfer an electron to the TiO$_2$ CB or, alternatively, can transfer an electron to a TiO$_2$ surface state (TiO$_2$-ss). While the latter case results in a charge loss, the former case can lead to electrical work if the charge is transported efficiently to the contact. However, it is also likely that the electron can undergo back electron transfer to the MAPI perovskite or to the spiro-OMeTAD film. Last but not least, it is also feasible that upon light excitation and carrier generation an electron can be directly transferred from the MAPI perovskite CB to the HTM spiro-OMeTAD. Scheme 1 shows a representation of the interfacial charge transfer described above. Needless to say that we have not included other charge transfer reactions (ie: radiative and non radiative charge transfer reactions within the MAPI perovskite) to simplify the graphical representation.

Interfacial electron transfer reaction (4) in Scheme 1 is still under debate as it implies that electrons must be transported through the perovskite material to recombine with holes at the HTM, in this case the spiro-OMeTAD.[24] This process can be possible if charges have excellent mobility at the MAPI perovskite and also may occur if the perovskite overlayer on top of the mpTiO$_2$ presents micropores where the spiro-OMeTAD can penetrate and get closer to the TiO$_2$. In any case, early work by Moser and co-workers have already measured this electron transfer reaction, which supposes a non radiative carrier recombination pathway that minimised the solar cell efficiency[25]. Yet, we must consider that these measurements and the ones described herein below are registered in dark conditions (without any light bias) and may differ from charge transfer reactions under light irradiation conditions[26].

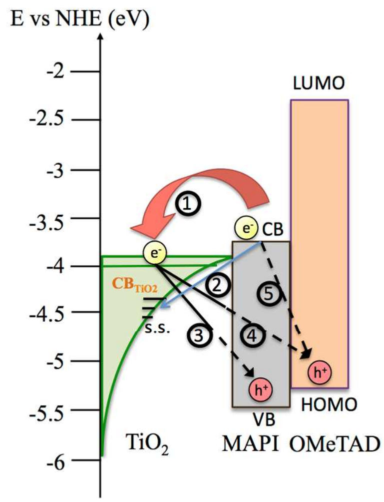

Scheme 1. Interfacial charge transfer reactions upon light excitation in mpTiO_2/MAPI/spiro-OMeTAD. (1) Electron injection from the MAPI perovskite CB to the TiO_2 CB. (2) Charge transfer from the MAPI perovskite CB to the TiO_2 surface states. (3) Back-electron transfer from the TiO_2 to the MAPI perovskite VB (valence band). (4) Back-electron transfer from the TiO_2 to the spiro-OMeTAD and (5) electron transfer from the MAPI perovskite to the spiro-OMeTAD.

Figure 4 shows the IR L-TAS interfacial charge recombination reaction, reaction 4 at Scheme 1, for our different mpTiO_2/MAPI/spiro-OMeTAD thin films. We registered the measurement at λ_{probe}=1400nm that corresponds to the wavelength near the maximum absorption of the spiro-OMeTAD positive polarons (spiro-OMeTAD$^+$) as reported before.[24] Figure 5 illustrates the IR L-TAS spectrum for the mpTiO_2/MAPI/spiro-OMeTAD upon excitation at λex=580nm under nitrogen at 25^o C.

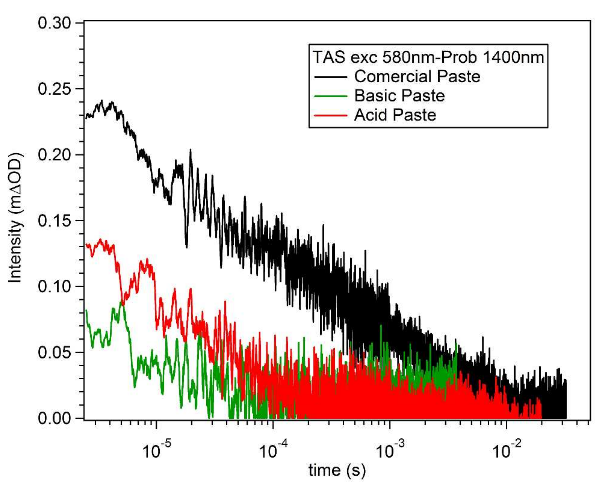

Figure 4 Photo-induced interfacial charge recombination decays for the mpTiO_2 acid (red), mpTiO_2 basic (green) and the mpTiO_2 commercial pastes with the MAPI perovskite and the spiro-OMeTAD layers alike in a functional solar cell. The excitation wavelength was λ_{ex}=580nm and the probe wavelength was λ_{probe}=1400nm.

As can be seen in Figure 4, the most striking observation is the low signal amplitude for the basic mpTiO_2 sample in comparison with the acid mpTiO_2 and the commercial mpTiO_2 paste. As all samples have alike absorption at 580nm, this results implicates that for the basic mpTiO_2 there is much less yield of electron injection from the MAPI perovskite to the TiO_2 CB. On the contrary, the signal amplitude for the commercial mpTiO_2 /MAPI/spiro-OMeTAD film denotes a greater yield for the electron injection (reaction 1 at Scheme 1) process.

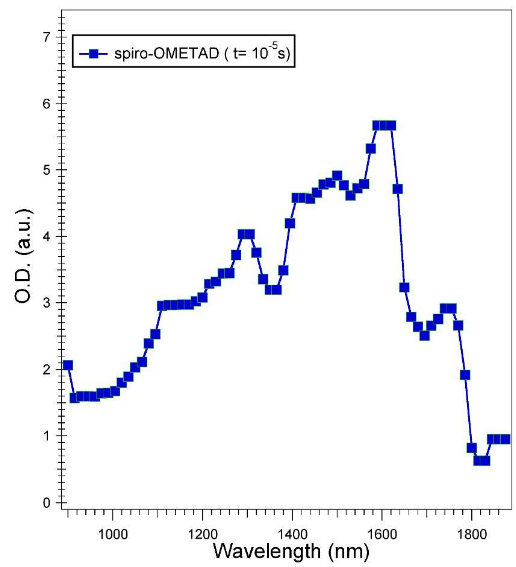

Figure 5. Photo-induced IR-LTAS spectrum for a mpTiO_2/MAPI/spiro-OMeTAD film (mpTiO_2 commercial) registered after 10 microseconds of laser excitation (laser power 70microJ/cm^2) at λex=580nm under ambient conditions.

The IR L-TAS measurements are in good agreement with the measurements carried out using TCSPC and shown in Figure 3, where the mpTiO_2/MAPI basic film shows the slowest radiative recombination decay for TiO_2 samples and the electron injection in this particular film is not efficient. Thus, we can establish that the order for efficient electron injection in our different mpTiO_2 films is commercial>acid>basic ncTiO_2 nanoparticles. Moreover, other important feature that can be seen in Figure 4 is the different decay half-lifetimes (measured at the decay half maximum of its signal amplitude) for the acid and the commercial mpTiO_2/MAPI/spiro-OMeTAD films. The former has a $\tau_{1/2}$=26µs and the later a $\tau_{1/2}$=170µs, respectively. As the laser power intensity was kept constant and the MAPI perovskite absorption at the excitation wavelength was alike the first hypothesis for the observed difference in decay lifetime is that the electrons at the acid mpTiO_2 are deeply trapped while in the commercial mpTiO_2 the electrons are in shallow traps and can more easily migrate to the surface.
To complete our study, we now turned into the fabrication and characterization of the MAPI perovskite solar cells using the different mpTiO_2 films.

MAPI perovskite solar cells characterization.

We fabricate the MAPI perovskite solar cells as detailed at the Experimental Section. Figure 6 shows the measured IV curves (current vs. voltage) under standard 1 sun measuring conditions (100mW/cm^2 sun-simulated 1.5.AM G spectrum)

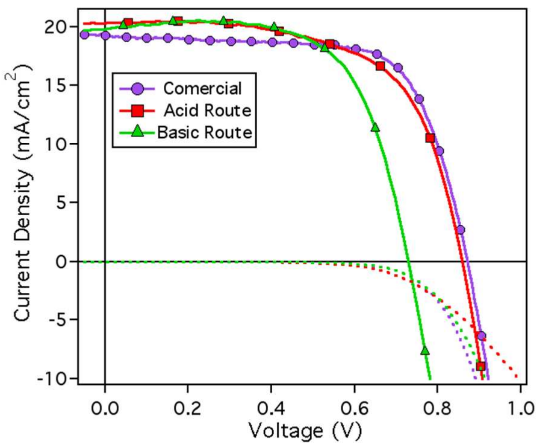

Figure 6. The current vs. voltage curves measured under 1sun (1.5 AM G sun simulated irradiation, lines with markers) and under dark in reverse bias with an integration time of 8 seconds and a delay time of 0 seconds. The solar cells have an area of 0.25cm2.

The most relevant parameters from the measured MAPI perovskite solar cells are listed in Table 2. The solar cells fabricated with the basic mpTiO_2 show almost identical Jsc (≈20mA/cm^2), however, the Voc (730mV) is systematically lower in these devices. On the other hand, the acid mpTiO_2 film shows almost alike performance as the commercial TiO_2 paste.

Table 2. Most relevant parameters for the MAPI perovskite solar cells measured in this work.

	Jsc (mA)	Voc (mV)	FF (%)	η (%)	Rs (Ω)	Rsh (Ω)
Basic	19.8	733	66.56	9.62	9	4.25e4
Acid	20.10	870	63.25	11.06	22	1.3e5
Com	19.35	870	69.14	11.64	6.6	8.1e4

Jsc= Photocurrent density. Voc = Open circuit voltage. FF=Fill Factor. η = Efficiency .Rs= Series Resistance. Rsh = Shunt resistance.

To study further the reasons for the differences between the acid and the basic mpTiO_2 films in MAPI perovskite solar cells we carried out, as detailed below, photo-induced time resolved advanced spectroscopy such as PIDC and PIT-PV.

Photo-induced differential charging (PIDC) and photo-induced transient photo-voltage (PIT-PV)

The PIDC technique has been previously applied in OPV and QDSC (quantum dot solar cells) and more recently in MAPI perovskite solar cells to measure the charge density at different light bias[17]. As can be seen in Figure 7 the PIDC data at different light bias leads to a different exponential distribution of the charges. The PIDC data is the result of the accumulated charge at the different materials including the mpTiO_2, the MAPI perovskite and the HTM.

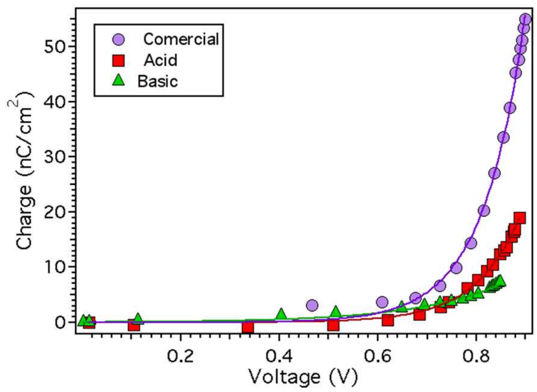

Figure 7. Charge measured using PIDC at different light bias for the different mpTiO_2 MAPI perovskite solar cells.

In previously mpTiO_2 based MAPI perovskite solar cells PIDC was correlated to the electronic charge at solar cell and, moreover, it was possible to obtain the recombination current value Jrec for the devices with good agreement with the measured Jsc. However, the Jrec values were only meaningful when the fastest component of the PIT-PV decay was considered.

We carried out the PIT-PV measurements (Figure 8), as described before, leaving the MAPI solar cell under different illumination intensities to stabilize its Voc.

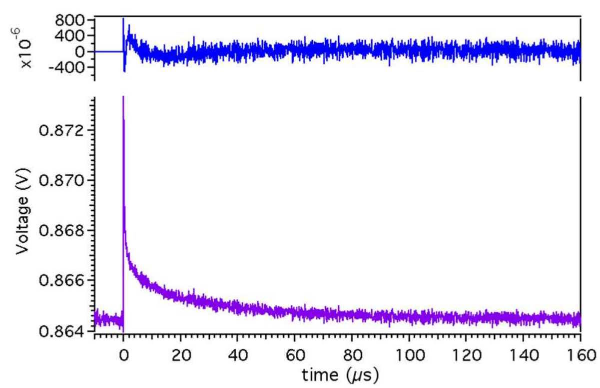

Figure 8. The PIT-PV decay at 1sun (solar cell Voc= 0.870V) for the MAPI solar cells fabricated using the commercial mpTiO_2. The top figure shows the residual plot for the decay fitting to a bi-exponential equation.

For all MAPI solar cells, independently of the mpTiO_2 used the PIT-PV decay cannot be fitted to a single mono-exponential equation but to a double-exponential equation instead. These results are in good agreement with previous measurements.[17, 19]

In Figure 9, we compare the fastest component of the PIT-PV decay at the same charge measured by PIDC.

As can be seen, the slowest decay lifetime corresponds to the commercial mpTiO_2 MAPI perovskite solar cells in clear contrast with the basic TiO_2 based devices.

On the one hand, the faster lifetime component of the decay for the basic mpTiO_2 MAPI perovskite solar cells can explain the lower Voc observed for these devices. This fast component is related to the electronic charge in the solar cell and the carrier recombination kinetics. Moreover, the slope of the charge vs. the decay lifetime for the basic mpTiO_2 (α = 2.4) implicates that small changes on the light bias leads to a greater increase of the decay kinetics in comparison with the acid or the commercial mpTiO_2 MAPI perovskite solar cells, which present an α= 0.96 and α= 0.7 respectively. On the other hand, the charge vs. decay lifetime for the acid mpTiO_2 MAPI perovskite solar cell is not much different when compared to the commercial mpTiO_2 device, which is in good agreement with the measured Voc (Figure 6).

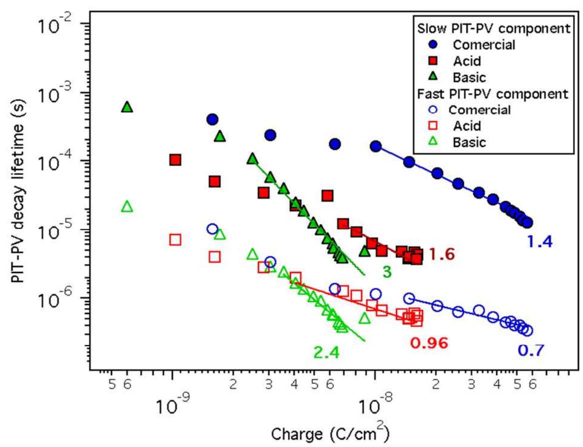

Figure 9. Charge vs. PIT-PV decay lifetimes. Filled and empty symbols correspond to the slow and the fast decay components, respectively.

Conclusions

In overall, we have demonstrated that different synthetic routes to achieve nanocrystalline TiO_2 nanoparticles lead to substantial differences in the solar-to-energy conversion efficiency of mesoporous TiO_2/ MAPI based solar cells. The differences observed are more accentuated in the solar cells open-circuit voltage value. A complete study of the charge transfer reactions in complete devices, illustrates that for the solar cells based on the mpTiO_2 from the basic route the electron transfer from the MAPI conduction band to the TiO_2 conduction band is less favoured. This can be understood in terms of TiO_2 conduction band energy position. It is well established that the TiO_2 conduction band can be shifted towards higher energy values, which makes the charge transfer less favourable. For example, in DSSC the use of pyridine in the liquid electrolyte shifts the TiO_2 CB and decreases the electron injection from the dye excited state (and hence the device photocurrent). In MAPI solar cells, since MAPI can transport effectively electrons and holes within the same material, there is no need of mesoporous TiO_2 to transport the electrons to the contact. Thus, even though the electron transfer process is less efficient in the basic TiO_2 it is still feasible to achieve high currents alike in Al_2O_3 mesoporous based MAPI solar cells[27]. This result is further confirmed by L-TAS where the decay amplitude, which is related to the population of polarons in the spiro-OMETAD as a result of the charge transfer process between the MAPI and the spiro-OMETAD, is also much lower for the basic mpTiO_2/MAPI solar cell.

Moreover, the analysis of the charges at the solar cells, under different illumination conditions using PIDC, shows that for a given voltage, close to sun-simulated illuminations of 1 sun, the acid and the basic mpTiO_2 show similar values in contrast to the commercial mpTiO_2/MAPI that has higher charge density. In other type of solar cells[28], the accumulated charge is related to the splitting of the quasi Fermi levels in the different materials that lead to the solar cell junction. The energy difference between the quasi Fermi levels is directly related to the solar cell open-circuit voltage. Hence, the more charge accumulated, the greater the difference in energy between the quasi Fermi levels and higher is the Voc. Furthermore, the analysis of the PIT-PV decay kinetics (Figure 9) indicates that it is faster for the basic TiO_2, when comparing the data at the same charge density, and these faster kinetics are related to the lower measured Voc because the analysis of the charge density for the acid and the basic TiO_2 (Figure 7) shows that are almost identical despite the larger Voc measured for the acid TiO_2. Thus, we have demonstrated that the efficiency of MAPI solar cells, based on mesoporous TiO_2, not only depends on the MAPI itself as photoactive material but also on the nature of the TiO_2 nanocrystalline particles that effects important changes on the interfacial charge transfer process that limit the solar cell efficiency.

Acknowledgements

The authors thank MINECO (project CTQ2013-47183) as well as the Severo Ochoa Excellence Accreditation 2014-2018 (SEV-2013-0319). EP is also grateful to ICIQ and ICREA for economical support.

References

1. P. P. Boix, K. Nonomura, N. Mathews and S. G. Mhaisalkar, *Materials Today*, 2014, **17**, 16-23.
2. P. Gao, M. Gratzel and M. K. Nazeeruddin, *Energy Environ. Sci.*, 2014, **7**, 2448-2463.
3. K. T. Ramakrishna Reddy, N. Koteswara Reddy and R. W. Miles, *Sol. Energ. Mat. Sol. Cells*, 2006, **90**, 3041-3046.
4. H. Katagiri, K. Jimbo, W. S. Maw, K. Oishi, M. Yamazaki, H. Araki and A. Takeuchi, *Thin Solid Films*, 2009, **517**, 2455-2460.
5. R. E. Smalley, *MRS Bulletin*, 2004, **30**, 412-417.
6. C. Kim, S. Ryu, J. Seo and S. I. Seok, *Science*, 2015.
7. S. D. Stranks and H. J. Snaith, *Nat. Nano.*, 2015, **10**, 391-402.
8. K. Nakata and A. Fujishima, *J. Photochem. Photobiol. C: Photochem. Rev.*, 2012, **13**, 169-189.

9. A. Haidry, P. Schlosser, P. Durina, M. Mikula, M. Tomasek, T. Plecenik, T. Roch, A. Pidik, M. Stefecka, J. Noskovic, M. Zahoran, P. Kus and A. Plecenik, *Centr.Eur.J.Phys.*, 2011, **9**, 1351-1356.
10. S. Mathew, A. Yella, P. Gao, R. Humphry-Baker, F. E. CurchodBasile, N. Ashari-Astani, I. Tavernelli, U. Rothlisberger, K. NazeeruddinMd and M. Grätzel, *Nat. Chem.*, 2014, **6**, 242-247.
11. B. O'Regan and M. Gratzel, *Nature*, 1991, **353**, 737-740.
12. S. Hore, E. Palomares, H. Smit, N. J. Bakker, P. Comte, P. Liska, K. R. Thampi, J. M. Kroon, A. Hinsch and J. R. Durrant, *J. Mat. Chem.*, 2005, **15**, 412-418.
13. F. Fabregat-Santiago, J. Garcia-Canadas, E. Palomares, J. N. Clifford, S. A. Haque, J. R. Durrant, G. Garcia-Belmonte and J. Bisquert, *J. Appl. Phys.*, 2004, **96**, 6903-6907.
14. E. Palomares, J. N. Clifford, S. A. Haque, T. Lutz and J. R. Durrant, *J. Am. Chem. Soc.*, 2003, **125**, 475-482.
15. Q. Xue, Z. Hu, C. Sun, Z. Chen, F. Huang, H.-L. Yip and Y. Cao, *RSC Advances*, 2015, **5**, 775-783.
16. J. H. Heo, H. J. Han, D. Kim, T. K. Ahn and S. H. Im, *Energy Environ.Sci.*, 2015, **8**, 1602-1608.
17. B. C. O'Regan, P. R. F. Barnes, X. Li, C. Law, E. Palomares and J. M. Marin-Beloqui, *J. Am. Chem. Soc.*, 2015, 5087-5099.
18. J.-H. Im, C.-R. Lee, J.-W. Lee, S.-W. Park and N.-G. Park, *Nanoscale*, 2011, **3**, 4088-4093.
19. J. M. Marin-Beloqui, J. P. Hernandez and E. Palomares, *Chem. Comm.*, 2014, **50**, 14566-14569.
20. K. Suttiponparnit, J. Jiang, M. Sahu, S. Suvachittanont, T. Charinpanitku and P. Biswas, *Nanoscale Res. Lett.*, 2011, **6**, 1-8.
21. M. De Bastiani, V. D'Innocenzo, S. D. Stranks, H. J. Snaith and A. Petrozza, *APL Materials*, 2014, **2**, 081509.
22. V. Roiati, S. Colella, G. Lerario, L. De Marco, A. Rizzo, A. Listorti and G. Gigli, *Energy Environ. Sci.*, 2014, **7**, 1889-1894.
23. Y. Yamada, T. Nakamura, M. Endo, A. Wakamiya and Y. Kanemitsu, *J. Am. Chem. Soc.*, 2014, **136**, 11610-11613.
24. F. T. F. O'Mahony, Y. H. Lee, C. Jellett, S. Dmitrov, D. T. J. Bryant, J. R. Durrant, B. C. O'Regan, M. Graetzel, M. K. Nazeeruddin and S. A. Haque, *J. Mat. Chem. A*, 2015, **3**, 7219-7223.
25. A. Marchioro, J. Teuscher, D. Friedrich, M. Kunst, R. van de Krol, T. Moehl, M. Gratzel and J.-E. Moser, *Nat. Photon.*, 2014, **8**, 250-255.
26. R. Gottesman, L. Gouda, B. S. Kalanoor, E. Haltzi, S. Tirosh, E. Rosh-Hodesh, Y. Tischler, A. Zaban, C. Quarti, E. Mosconi and F. De Angelis, *J. Phys. Chem. Lett.*, 2015, **6**, 2332-2338.
27. M. M. Lee, J. Teuscher, T. Miyasaka, T. N. Murakami and H. J. Snaith, *Science*, 2012.
28. J. Bisquert and G. Garcia-Belmonte, *J. Phys. Chem. Lett.*, 2011, **2**, 1950-1964.